Image Reconstruction Using Bispectrum Speckle Interferometry: Application and First Results

Roberto Maria Caloi
Unione Biellese Astrofili, Italy
robime@iol.it

Abstract: Speckle interferometry yields diffraction-limited information from sequences of atmospherically-degraded short-exposure images. Sophisticated algorithms have been proposed by astronomers to reconstruct the actual image of an object. The reconstructed images allow one to measure the relative positions and the magnitude differences of the stars in a multiple star system up to the resolving power of the available instrumentation. Here I report on the main measurements and analysis required to apply one of these techniques, the building block method using the bispectrum. Preliminary results obtained with simulations and using a small telescope are shown.

1. Introduction

The atmospheric turbulence limits the resolving power of a telescope, including the smaller ones usually available to amateur astronomers, when observing with typical seeing conditions. In the last decades, professional astronomers have developed several techniques to extract as much information as possible from their sophisticated instrumentation, with speckle interferometry and recently adaptive optics most commonly used. While the latter technique is available only in the most advanced observatories in the world, the former can be applied by a much broader community, including amateur astronomers in the most simple set-ups, both for scientific and educational purposes (Genet, 2015).

In my previous paper on this subject (Caloi, 2008), I reported on an application of speckle interferometry to the estimation of the separation and position angle of double stars using the Directed Vector Autocorrelation method (Bagnuolo et al., 1992). Regarding the relative brightness of the two components in a binary star, methods that are essentially parametric are also available (Glindemann et al., 1992). As an amateur astronomer, I have been nevertheless attracted by the idea of getting a full image of the object under study. Even if parametric methods require much less computing time and yield all the information as well, when the nature of the object under study is well known, as in the case of a binary star, an image is necessary when dealing with more complex or simply unknown objects, as in the case of multiple star systems or diffuse structures.

After reviewing the existing literature and, I must say, significantly underestimating the effort needed to understand all the steps required to replicate the algorithm, I decided to implement the iterative building block method (Hofmann and Weigelt, 1993). This data reduction technique is based on the statistical properties of the bispectrum of the atmospherically degraded optical transfer function of a telescope (Lohmann et al., 1983). For a detailed review on the state of the art in the more general field of optical interferometry applied to the image reconstruction problem, I refer the reader to the recent tutorial of Thiébaut and Young (2017).

The main purpose of this paper is to highlight the key aspects as well as some of the issues that, at least for me, were initially quite difficult to familiarize with, so that other amateur astronomers could have a starting point before reading the original papers, where the theory and limitations of the methods and formulas reviewed here are covered in detail.

For rapid prototyping and deployment of all required calculations, I have used Matlab, which has provided me a very good compromise between performance and ease of development.

2. Image Formation

The image reconstruction process is essentially an inverse problem, since the main task is to recover the

original image based on the result of observations. Several noise sources make the recovering process subject to uncertainties and biases. In order to appreciate all the data and assumptions necessary to deal with these aspects, it helps to review the main physical processes involved in the image formation on the detector that are later considered to recover the original image. Other refinements could be evaluated, in particular on how to model the actual functioning of a real detector, but they are not considered here.

The near axis image formation process can be described as follows (Klein and Furtak, 1986). Let us consider a point-like monochromatic optical source, like a single star observed using a narrow-band filter, located in the ideal source plane at position (x', y') at a large distance R'_0 from the telescope, thus forming a small angle

$$\frac{\sqrt{x'^2+y'^2}}{R'_0}$$

with respect to the telescope optical axis. The resulting electric field intensity on the image plane, where the detector is located, is proportional to the Fourier transform of the transmission function $\tau(\tilde{x}, \tilde{y})$ defined on the telescope aperture plane. The transmission function summarizes the combined effects of the telescope aperture, its aberrations and the atmospheric disturbances. The resulting intensity distribution on the image plane can be represented as a function $PSF^{\lambda}(x, y)$ (the so called *point spread function* at wavelength λ) centered on (fx'/R'_0, fy'/R'_0), where f is the actual focal length of the telescope. The image formed by the telescope on the detector is thus located in the position that is expected by geometrical optics, and spread according to the PSF. In the case of an extended incoherent optical source with an intensity distribution $o(x,y)$ according to geometrical optics, the actual image intensity distribution $i^{\lambda}(x, y)$ is the convolution of $o(x, y)$ with the point spread function $PSF^{\lambda}(x,y)$.

$$i^{\lambda}(x,y) = o(x,y) * PSF^{\lambda}(x,y) \qquad [1]$$

Equation 1 holds in the isoplanatic approximation, i.e. when the spread function does not change in the region of interest, and if the emission from the source object is not coherent, as is the case with the light emitted from a star. Under ideal conditions the point spread function for a given wavelength λ would depend on the telescope only but, due to the atmospheric turbulence, the transmission function $\tau(\tilde{x}, \tilde{y})$ changes rapidly both in time and space and, as a consequence, the same happens to $PSF^{\lambda}(x,y)$. Thus, the actual intensity distribution $i_t^{\lambda}(x, y)$ at each time t depends on a different point spread function $PSF_t^{\lambda}(x,y)$ such that

$$i_t^{\lambda}(x,y) = o(x,y) * PSF_t^{\lambda}(x,y) \qquad [2]$$

Given the incoming intensity distribution $i_t^{\lambda}(x, y)$, the actual number of photons detected per pixel will depend also on the quantum nature of light and on the actual detector used, whose main characteristics are the following: level of dark current generation, quantum efficiency, electronic read-out noise, electronic biases, presence of defects and hot pixels. These effects are particularly important when the average total number of detected photons per speckle N^{ph} is low, some hundreds or thousands to give an order of magnitude, and must be dealt with in order to avoid estimation biases (which do not disappear by simply increasing the number of recorded images used in the data reduction process).

If $i_t^{\lambda}(x, y)$ is normalized so that its total value over the image plane is one, the expected number of photoelectrons $i_t^{phe}(x,y)$ is then given by

$$i_t^{phe}(x,y) = N^{ph}\left[o(x,y) * PSF_t^{\lambda}(x,y)\right] + n_{th} \qquad [3]$$

where n_{th} represents the contribution of thermally generated electrons, here assumed to be independent from the pixel location.

The actual number of generated photoelectrons $P(i_t^{phe}(x,y))$ follows a Poisson distribution with average given by $i_t^{phe}(x, y)$. The subsequent mechanism of charge shift and amplification typical of CCDs, introduces an additional noise component, the so called read-out noise, which can be represented by a random variable normally distributed with zero mean and variance σ_e^2, indicated in what follows by $N(0, \sigma_e^2)$. An additional time invariant bias $b_{DC}(x, y)$ and a spatial dependent sensitivity factor $l(x, y)$ are also normally taken into account (due to electronic bias, defects and hot pixels, dust, etc.). The final digital value (ADU) recorded for each pixel is obtained by summing all three previous components and dividing by the detector gain G,

$$i_t^{ADU}(x,y) = \begin{bmatrix} P\left(i_t^{phe}(x,y)\right) l(x,y) + N\left(0,\sigma_e^2\right) + \\ b_{DC}(x,y) \end{bmatrix} \left(\frac{1}{G}\right) \qquad [4]$$

where i_t^{ADU} (x,y) represents the detected specklegram at time t.

Equations 3 and 4 provide a simplified representation of the detection process, and they have been used for the actual implementation of the data-reduction process of this work. In the following sections, position (x,y) will be denoted by x to simplify expressions, with the understanding that x is the pixel bi-dimensional position.

3. Power Spectrum Estimation

A data cube $\{i_t^{ADU}(x)\}^M_{t=1}$ of M short exposure frames (specklegrams) of the object is the starting point of the analysis. A similar data cube $\{d_t^{ADU}(x)\}^L_{t=1}$ obtained with the telescope aperture covered is needed. The first step in the image reconstruction process requires the computation of the power spectrum, both its average and variance. Each frame $i_t^{ADU}(x)$ is first corrected for the gain, G, the bias $b_{DC}(x)$ and the flat field $l(x)$, to yield the actual photo-electrons plus read-out noise per pixel

$$i_t(x) = \frac{G i_t^{ADU}(x) - b_{DC}(x)}{l(x)}$$

It is subsequently cropped within a square frame centered at the position corresponding to the speckle moving average maximum intensity. The frame size is chosen large enough to contain the entire speckle, with each side made by a number of pixels equals to a power of two, in order to reduce the computation time of subsequent applications of the Fast Fourier Transform algorithm. The total number of photo-electrons and thermal electrons per frame $N_t = N_t^{ph} + N_t^{th}$ is also computed. The same cropped regions are used with the dark frames sequence to compute the total dark current due to the thermally generated electrons N_t^{dth} per frame. Here we assume that N_t^{th} and N_t^{dth} have the same expected values.

The discrete Fourier transform $I_t(u) = DFT(i_t(x))$ where u indicates the bi-dimensional frequency component, is performed for each specklegram. It has been shown (Goodman et al., 1976) that at low light levels, a typical situation in speckle interferometry, the computed power spectrum must be compensated for biases due to the photon noise inherent in the detection process. Gordon and Buscher (2012) derived a formula for a bias-free power spectrum estimator $S_t(u)$, when photon noise, thermal noise (dark current), and read-out noise are all taken into account. The main stated assumption in their study is that the various noise sources considered are independent and additive. Moreover the overall noise on different pixel positions is assumed to be statistically independent.

Under discrete Fourier transform conditions, which hold in our case, their proposed estimator becomes

$$S_t(u) = |I_t(u)|^2 - \sum_x \left(i_t(x) + \sigma_e^2(x) \right) \qquad [5]$$

where x indicates the pixel position, $i_t(x)$ the recorded intensity, and $\sigma_e^2(x)$ is the read-out noise variance. Under the additional assumption that the read-out noise does not depend on the detector position, i.e. $\sigma_e(x) = \sigma_e$, equation 5 becomes

$$S_t(u) = |I_t(u)|^2 - N_t - N_{pix}\sigma_e^2 \qquad [6]$$

where $N_t = N_t^{ph} + N_t^{th}$ is the total number of photo-electrons and thermal electrons per frame and N_{pix} is the total number of pixels. By averaging $S_t(u)$ we obtain an unbiased estimate of the power spectrum

$$S = \left\langle |I(u)|^2 \right\rangle - \langle N \rangle - N_{pix}\sigma_e^2 \qquad [7]$$

where the operator ‹› represents averaging over the entire sequence of specklegrams. The sample variance of such estimate $var(S)$ is then used to calculate the frequency dependent power spectrum standard deviation $\sigma_S(u)$,

$$\sigma_S(u) = \sqrt{\mathrm{var}\left(S(u)\right) / M} \qquad [8]$$

where M is the number of frames. The resulting power spectra has a central peak which is given by $(\tilde{N}^{ph} + \tilde{N}^{th})^2$ where $\tilde{N}^{ph}$ is the average number of photo-electrons per frame and $\tilde{N}^{th} = \tilde{N}^{dth}$ is the average number of electrons generated by the thermal noise. By correcting the central peak component for the thermal noise, the final estimate of the power spectrum $S(u)$ is obtained. No further correction is necessary outside the central peak if the thermal noise is spatially uncorrelated, so that its power spectrum is negligible for spatial frequencies different from zero.

The same analysis just described is repeated for a nearby reference star, which must be observed with similar seeing conditions as the object under study. Once we have estimated the object power spectrum $S_{obj}(u)$ and its variance $\sigma^2_{Sobj}(u)$ as well as the reference star's power spectrum $S_{ref}(u)$ and its variance $\sigma^2_{Sref}(u)$, we can apply the standard procedure of speckle interferometry (Labeyrie, 1970) which yields an estimate of the true object power spectrum $|O(u)|^2 = S_{obj}(u)/S_{ref}(u)$ up to the telescope cut-off frequency, and its variance $\sigma^2_{|O(u)|^2}$

$$\frac{\sigma^2_{|O(u)|^2}}{|O(u)|^2} = \left[\frac{\sigma_{S_{obj}}(u)}{S_{obj}(u)}\right]^2 + \left[\frac{\sigma_{S_{ref}}(u)}{S_{ref}(u)}\right]^2 \quad [9]$$

The power spectrum $|O(u)|^2$ does not contain any information regarding the phase $\varphi(u)$ of an object visibility $O(u) = |O(u)|\ e^{i\varphi(u)}$, from which the image could be reconstructed by applying the inverse Fourier transform. As a consequence, it cannot be used alone to recover an object image without some prior information about the object itself. The bispectrum is one observable quantity that contains such information.

4. Bispectrum Estimation

Let us first recall its definition. Given an intensity distribution $i(x)$ and its Fourier transform $I(u)$, the bispectrum is defined as $I^{(3)}(u,v) = I(u)I(v)I^*(u+v)$, where $I^*(u)$ indicates the complex conjugate of $I(u)$. Similarly, for the true object intensity distribution $o(x)$ we have $O^{(3)}(u, v) = O(u)O(v)O^*(u + v) = |O^{(3)}(u,v)| \exp[\beta_{O(3)}(u,v)]$. It has been shown by Lohmann et al. (1983) that the phase of the time-averaged bispectrum of the atmospheric transfer function is close to zero while its modulus is not and, as a consequence, the phase of the observed average bispectrum $\beta_{I(3)}(u,v)$ is equal to the phase of the object bispectrum $\beta_{O(3)}(u,v)$. This relation holds for $|u|$, $|v|$, and $|u + v|$ smaller than the telescope cut-off frequency. They also describe an iterative computation to recover $\varphi(u)$ from $\beta_{O(3)}(u,v)$. This property highlights the importance of the bispectrum for image reconstruction.

Astronomers have also investigated in detail how to take into account the effects of the photon noise (Wirnitzer, 1985) on its measurement. These effects lead to a bias that is significant at low light levels, when the number of photons detected per frame is of the order of less than some thousands. A bias cannot be overcome by simply increasing the number of detected interferograms. If compared to the variance, its significance becomes greater when the number of samples used to compute the average increases.

In what follows, I report the formulas presented by Gordon and Busher (2012). They extend the original results of Wirnitzer for the bispectrum, to the case where several additive noise sources are significant at the same time in the general framework of optical interferometry.

In our case, the DFT conditions stated in their paper apply. Moreover, assuming that the read-out noise does not depend on the pixel position, the given unbiased estimator reduces to

$$B_t(u,v) = I_t(u)I_t(v)I_t^*(u+v) - |I_t(u)|^2 - |I_t(v)|^2 - |I_t(u+v)|^2 + 2N_t + 3N_{pix}\sigma_e^2 + C * \delta(u,v) \quad [10]$$

$$C = -3N_t N_{pix}\sigma_e^2$$

where, following the same convention used in the previous section, $N_t = \Sigma_x i_t(x)$ is the total number of photoelectrons and thermal electrons recorded per frame, N_{pix} is the total number of pixels, and σ_e^2 is the read-out noise variance. By averaging (10) over t, we obtain an unbiased estimate of the bispectrum.

Finally, taking into account (6), we get

$$\langle B(u,v)\rangle = \langle I(u)I(v)I^*(u+v)\rangle - |S(u)|^2 - |S(v)|^2 - |S(u+v)|^2 - \langle N\rangle + C * \delta(u,v) \quad [11]$$

We can now combine the object's visibility modulus $|O(u)|$, obtained as described in the previous section, and the bispectrum phase (also called closure phase) $\beta(u, v) = arg(< B(u, v) >)$ to obtain our estimate of the object's bispectrum

$$O^{(3)}(u,v) = |O(u)||O(v)||O(u+v)|e^{i\beta(u,v)} \quad [12]$$

5. Image Reconstruction

We can now proceed to search for the object's image, whose bispectrum shows the best agreement with the unbiased average bispectrum obtained as described in the previous section.

The algorithm used here is the *building block method* (BBM) and the details are provided in the original paper by Hofmann and Weigelt (1993). An improved algorithm for the same purpose and based on similar considerations was proposed later by the same authors (Hofmann et al., 2014)

The main idea of the building block method is to reconstruct the object's image iteratively, by modifying the initial guess by adding one block at a time. Each new block position is chosen in such a way to reduce the distance d_k, also called cost function, between the bispectrum of the new image after k iterations $O_k^{(3)}(u, v)$ and the measured bispectrum $O^{(3)}(u, v)$. The process is repeated until the distance is minimized according to a given stopping rule.

In the building block method the user can choose among different metrics in order to define a goodness of fit. The approach followed here does not include any regularization technique and implements the following definition of distance d_k.

$$d_k = \int \frac{\left| O_k^{(3)}(u,v) - O^{(3)}(u,v) \right|^2}{\sigma^2_{O^{(3)}(u,v)}} du\, dv \qquad [13]$$

which assigns a greater weight to those regions where the variance in the measured data is lower and where the integral represents summation over the 4-dimensional bispectrum support. As given in Appendix A of Hofmann et al. (2014), one source of uncertainty depends on the estimated power spectrum and it translates into an uncertainty in the bispectrum modulus as

$$\sigma_{\left|O^{(3)}(u,v)\right|} = 0.5\sqrt{S(u)S(v)S(u+v)} \cdot \sqrt{\frac{\sigma_S^2(u)}{S^2(u)} + \frac{\sigma_S^2(v)}{S^2(v)} + \frac{\sigma_S^2(u+v)}{S^2(u+v)}} \qquad [14]$$

which holds for small relative errors.

The second source of uncertainty comes from the phase of the estimated object bispectrum, whose variance $\sigma^2_{\beta(u,v)}$ can be calculated conveniently as described in Glindemann et al. (1992) and Gordon et al. (2012) as the variance of the projection of each frame's bispectrum on a direction perpendicular to their average, divided by the square of their average modulus and the number of frames. I have considered other angular dispersion measures based on directional statistics, as well as an approach based on the bootstrap method, but a preliminary investigation has not resulted in improved results so far.

Regarding the value of the variance required by the weight factor in the cost function used in the building block method, several approaches are possible. The approach used here is to consider the bispectrum modulus and phase as two independent random variables. In this case, the bispectrum variance can be approximated by

$$\sigma^2_{O^{(3)}(u,v)} = \sigma^2_{\left|O^{(3)}(u,v)\right|} + \left|O^{(3)}(u,v)\right|^2 \sigma^2_{\beta(u,v)} \qquad [15]$$

which holds when both modulus and phase variances are relatively small. A better approximation, which takes into account the wrapping effect in the complex plane, is presented in Hofmann et al. (2014), but has not been used for the preliminary results reported in the following sections.

Pauls *et al*., (2005) propose a different model, where $\sigma^2_{|O^{(3)}(u,v)|}$ and $\sigma^2_{\beta(u,v)}$ are reported and used separately in order to arrive to a more general error model for the bispectrum.

As a matter of fact, I found the analysis of the quality of the reconstructed image as a consequence of different choices of the cost function to be an active field of research among professional astronomers in general and not only for the BBM. After initially trying several different versions of the building block cost function, with some changes in the final outcome of the reconstructed image, I have chosen expressions 13 to 15 for the actual implementation of the algorithm, mainly to reduce at the minimum the overall complexity needed to get a satisfactory outcome with the objects considered in this study, i.e. triple and binary stars.

Because the image is built by changing one pixel at a time, some details that are not consistent with the actual maximum resolving power of the telescope can be generated. To correct this outcome, the image resulting from the optimization process is smoothed by convolution with the known theoretical PSF of the telescope.

To sum up, the main steps required to carry out the image reconstruction by bispectrum speckle interferometry are:

- Estimate the object power spectrum and from that the modulus of the object visibility $|O(u)|$
- Estimate the object's bispectrum phase $\beta(u, v)$
- Combine the two previous results to get the object bispectrum $|O(u)||O(v)||O(-u - v)|e^{i\beta(u,v)}$ and its variance
- Fit the object bispectrum, the iterative building block is used here, to recover the object image taking into account the estimated uncertainty in the bispectrum according to a suitable cost function
- Smooth the resulting image with the theoretical PSF of the telescope to avoid super-resolution artifacts

6. Simulation

In order to verify the reconstruction procedure under controlled conditions, simulated specklegrams have been generated assuming a monochromatic source by replicating the main physical processes introduced in section 2. The simulation starting point is a multiple star system, represented by a bi-dimensional normalized intensity function $o(x)$,

$$o(x) = \frac{\sum_{i=1}^{n} A_i \delta(x - x_i)}{\sum_{i=1}^{n} A_i} \qquad [16]$$

where x_i represents the position and A_i the intensity of each star's component i. Imaging equation 1 is then used. The PSF of each simulated frame is generated using a complex transmission function with a modulus defined by the geometry of the telescope aperture (primary and secondary mirror diameters) and a phase $\varphi(\tilde{x},\tilde{y})$ dependent on the position in the entrance pupil, the phase screen, which represents the effect of the atmospheric turbulence. The algorithm used to generate the phase screen is based on the Fast Fourier Transform method (McGlamery, 1976). The FFT method computes the phase screen by means of the inverse Fourier transform of the product of a circular complex Gaussian random noise with zero mean and unit variance and the square root of the phase power spectrum density $W_\varphi(f)$. For this purpose we can use Kolmogorov's law for energy dissipation in a viscous medium

$$W_\varphi(f) = \frac{0.023}{r_o^{5/3} f^{11/3}} \qquad [17]$$

where r_o is the Fried's parameter. This model is assumed to hold for spatial frequencies $1/L_o < f < 1/l_o$, where L_o is the outer scale and l_o is the inner scale of turbulence. Other expressions for W_φ, for example the von Krmn model, as well as other improved methods have been proposed (Lane et al., 1992; Sedmak, 2014) to avoid some shortcomings of the Kolmogorov formula and to obtain simulations in better agreement with the actual effect of the atmospheric turbulence. I have not tried to implement them because their complexity would have taken me too far from the already challenging objective of this study, i.e. to replicate the image reconstruction algorithm using data acquired with an instrumentation setup typically accessible to an amateur astronomer.

For each frame a new random phase screen is generated and, from that, a new normalized PSF is obtained, which is then convolved with the object distribution intensity given by expression 16. Photon, thermal and read-out noise are subsequently added according to the processes already described in section 2. Finally, the image is modified according to a given uniform bias and divided by the detector gain to get a final specklegram according to expression 4.

7. Comparison to Simulated Data

The application of the previous simulation and data analysis steps to known objects through simulations, as well as the comparison with the results obtainable with other analysis methods in the special case of binary stars, has been very helpful to correct initial coding errors and to check the actual performance of my implementation of the image reconstruction algorithm.

The entire data reduction process can be roughly divided into two phases, i.e. power spectrum and bispectrum estimation, followed by the application of the building block method. When the object is known to be a binary star, the resulting separation (ρ), position angle (θ) and magnitude difference (Δm) can also be compared with the same parameters obtained by least mean square (LMS) fitting the power spectrum or the bispectrum. In these cases the weight factor is chosen to be equal to the reciprocal of, respectively, the variance of the power spectrum $\sigma^2_{S}(u)$ and the variance of the bispectrum $\sigma^2_{O^{(3)}(u,v)}$. For details on a similar method used for LMS fitting the bispectrum phase of a binary star, see Glindemann et al.(1992). The results of four simulations with known binary stars are given in Table 1. For each case, the known parameters are compared to those obtained using the building block method (BBM) and the parametric fitting of the power spectrum (PS) and bispectrum (BS). For reconstructed images, the luminosity of each star component is measured by summing the values of all the pixels surrounding the pixel with the maximum intensity. Telescope, filter and detector parameters are kept fixed and assumed equal to those given in Tables 2 and 3.

The results reported in Table 1 are not intended to be comprehensive, rather they give an idea of the many factors that influence the measurement outcome, in particular under extreme conditions (very close pairs, low brightness, bad seeing, high detector thermal and/or readout noise). Even changing the data analysis method has a substantial influence on the estimated values in these cases. When the simulated conditions are more favorable, the agreement among the different methods increases significantly. In general, I found the magnitude difference subject to a greater relative uncertainty compared to the separation and position angle. This observation is in agreement with similar considerations generally reported in the literature.

Considering that the main purpose of these comparisons was to check the correctness of the implemented data-reduction algorithm, and not to investigate the effectiveness and limits of an established image reconstruction technique, I found the agreement among different methods encouraging.

As an additional test and in order to verify the performance of the reconstruction algorithm with a more complex object, I considered also the case of a triple star with components AB and AC separated by 1.2 and 0.8 arcsec respectively, position angles $\theta_{AB}=23^o$,

Table 1. Binary star parameters estimated from 200 frames generated under different simulation conditions: (a) N^{ph}=30000, n_{th}=15, σ_e=10, b_{DC} =10, r_0=2.5 cm; (b) N^{ph}=3000, n_{th}=5, σ_e=7, b_{DC} =15, r_0=2.5 cm; (c) N^{ph}=1000, n_{th}=5, σ_e=7, b_{DC} =15, r_0=5.0 cm; (d) N^{ph}=500, n_{th}=2, σ_e=2, b_{DC} =5, r_0=5.0 cm

#	ρ (″)	θ (°)	Δm	ρ_{BBM} (″)	θ_{BBM} (°)	Δm_{BBM}	ρ_{PS} (″)	θ_{PS} (°)	Δm_{PS}	ρ_{BS} (″)	θ_{BS} (°)	Δm_{BS}
(a)	1.2	23	0.55	1.16	21.7	0.71	1.17	22.1	0.63	1.17	21.9	0.59
(b)	1.3	210	0.25	1.25	210.7	0.27	1.30	206.0	0.41	1.23	208.1	0.0
(c)	1.3	210	0.25	1.21	211.1	0.21	1.26	211.2	0.32	1.26	211.1	0.13
(d)	0.8	125	1.0	0.80	124.2	0.98	0.81	121.3	0.87	0.80	121.5	0.76

θ_{AC}=125°, and with a magnitude difference Δm_{AB}=0.55 and Δm_{AC}=0.99. An example of a specklegram simulated by using these parameters is shown in Figure 1. The estimated power spectrum, after bias subtraction and calibration is shown in Figure 2. As can be seen, the actual usable region is smaller than the theoretical maximum one given by the telescope cut-off frequency - which in this case corresponds to a circle with radius of about 15 pixels. It is the measured variance that gives the weight to assign to different regions when the data reduction process is carried out. The result is in any case sufficiently defined to be somewhat different, as expected, from the typical fringe pattern of a simple binary star. The image reconstructed using the building block method is shown in Figure 3. The estimated values of the magnitude differences from the reconstructed image are Δm_{AB}=0.54 and Δm_{AC} =0.97, which are very close to the actual values of the simulated object.

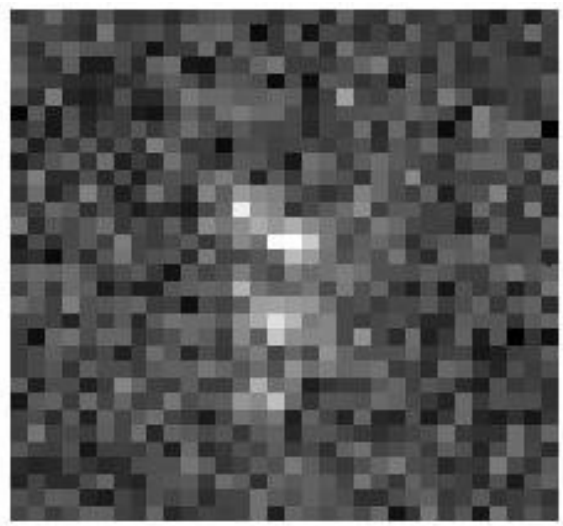

Figure 1: Example of specklegram of a triple star generated with simulation parameters N^{ph}=3000, n_{th}=10, σ_e=5, b_{DC} =15, r_0=3.0 cm. Image scale is 0.2171 arcsec per pixel.

8. Experimental Setup and Calibration

Speckle observations have been conducted with a 9.25" Schmidt-Cassegrain Celestron fitted with a JMI focuser and a Powermate 2.5X focal extender. The detector is an Imaging Source DMK 21AU04.AS based on a Sony ICX 098 BL chip, fitted with a Green Astronomik Type IIc filter. Nominal specifications for each component are summarized in Table 2.

The image reconstruction requires some input parameters that must be calibrated before the algorithm is executed. These estimates are given in Table 3.

The drift method (Caloi, 2008) is used to estimate the image scale and its orientation. Based on this calibration, the theoretical image cut-off frequency f_c is found to be 0.4594

$$f_c = \frac{D\Delta x}{\lambda f} = K\frac{D}{\lambda}$$

where D is the telescope primary diameter, Δx is the pixel size, f is the telescope effective focal length, λ is the effective transmission bandwidth center, which

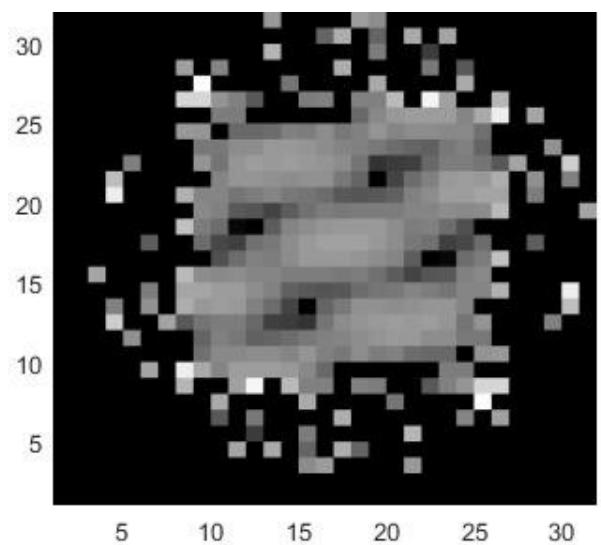

Figure 2: Estimated power spectrum (log scale) of a triple star from a sequence of 200 simulated specklegrams.

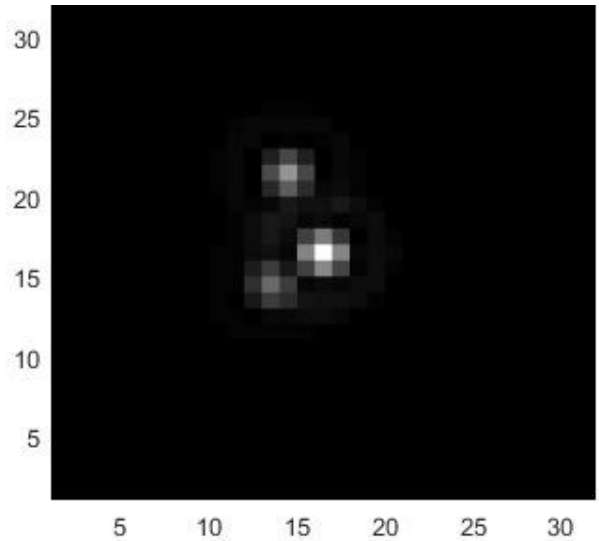

Figure 3. Reconstructed image of a simulated triple star.

combines the nominal filter properties and the frequency dependent quantum efficiency of the detector, and K is the image scale in rad/pixel. The cut-off frequency is less than 0.5, so this setup fulfills the Nyquist condition for digital image sampling.

Regarding the gain G of the CCD camera used in this study, the only related information I found on the producer website is the amplification scale which has a linear working range of 0 to 1023 corresponding to a 0 - 36 dB range (20 dB corresponds to an amplification factor of 10). Lacking such information, which is required if we want to apply the image reconstruction algorithm under low light conditions, I followed two different methods to estimate G as a function of the actual detector settings used during observations.

The first and less accurate method is based on the relation between the variance of a Poisson process with its mean, which gives

$$G\left(e^{-} / ADU\right) = \frac{\mu_c}{\sigma_c^2}$$

where μ_c and σ_c^2 are the mean and the variance respectively of the total counts, per given time interval, in a selected region of the detector with bright and uniform illumination, when photon noise is the main source of noise and the bias is negligible. The second method is less sensible to other noise sources or biases and requires measurement of μ_c and σ_c^2 as before under different light conditions. The gain is estimated as the slope of the linear regression of μ_c vs σ_c^2.

In addition, flat field images have been obtained

Table 2. Observation Nominal Parameters

Parameter	Symbol	Value
Telescope diameter	D	0.235 m
Telescope secondary obstruction	d	0.085 m
Transmission bandwidth	$\lambda \pm \Delta\lambda$	538 nm ± 40 nm
Pixel size (square shape)	$\Delta x \cdot \Delta x$	5.6 μm · 5.6 μm

Table 3. Calibrated parameters. Gain G is estimated for a nominal setting of 1023 on the DMK21AU04.AS CCD camera.

Parameter	Symbol	Value
Image scale	K	0.217 as/pixel
Detector gain	G	2.26 e^-/ADU
Theoretical cut-off frequency	fc	0.4594

to correct raw frames for non-homogenous spatial sensitivity, biases, or for the presence of dust on the detector's chip. Similarly, read-out and thermal noise have been estimated with the telescope aperture covered and with the same exposure time and CCD detector temperature of the actual observations of the target object and the reference star. A typical observing session requires, for each target object, obtaining several sequences of some hundreds of frames of both the target and the reference star, followed by similar sequences to estimate bias, dark current and read-out noise. I have used single frame exposure times in the 20-40 ms range, to *freeze* the speckle pattern, depending on seeing conditions and object brightness. The presence of a filter, the very short exposure time, and other practical considerations reduces significantly the possibility to successfully reconstruct the image of objects with a magnitude higher than 8 with the experimental setup used in this study.

9. Comparison to Measured Data

I have applied the image reconstruction procedure to video sequences captured during three different nights with the equipment already described in section 8. Due to the small size of the telescope, all objects considered have been binary stars. More complex objects, like close triple stars could become interesting targets if at least a medium size telescope with an aperture greater than 40 cm were used.

Even if seeing conditions were rather poor, 2 to 4 arcsec and windy, during all three observing

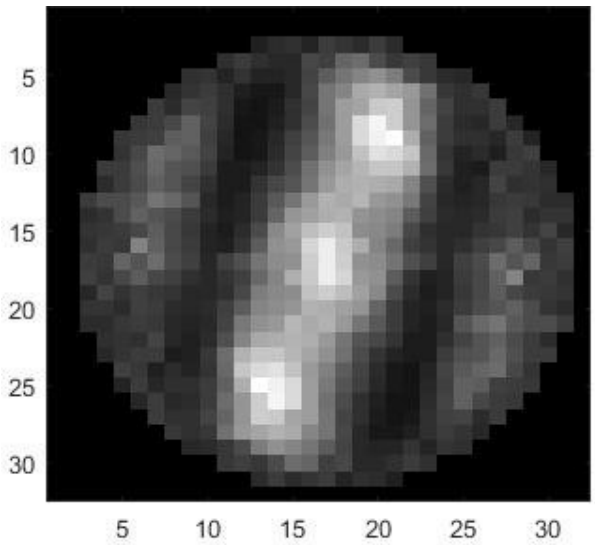

Figure 4: Average power spectrum of STF1909.

sessions, the high degree of atmospheric turbulence has facilitated the test of the performance of the reconstruction process, because speckles angular sizes were significantly greater than the resolving power of the telescope.

For each target, sequences of 200 up to 500 frames have been recorded and the measurements repeated during the same night. The dark current contribution was found to be negligible, while actual read-out noise was estimated to be between $3e^-$ and $7e^-$ depending on the chosen detector parameters and frame rate. Comparative results are given in Table 4 similarly to what has been done in Section 7 for simulated objects. Separations, position angles, and magnitude differences are extracted from the WDS catalog using the online search engine available at http://stelledoppie.goaction.it (Sordiglioni, 2012). Comparisons of measured magnitude differences to the known values must be considered indicative because the bandpass and center wavelength of the optical filter used in this study are just a proxy of a V-band standard filter. Moreover, the results obtained by model fitting the power spectrum (PS) and bispectrum (BS) are based on simple gradient descent minimization with a starting point given by the values obtained using the DVA method. As a consequence, the actual results could have been influenced by the presence of local minima in the optimization process.

Overall, the dispersion around known values for the magnitude differences is significantly greater than the errors in the separation and position angle, regardless of the method used. Nevertheless, these preliminary results confirm that the BBM yields reasonable estimates when compared to other methods applied to the same input data without *a priori* assumptions on the nature of the object under study.

The standard deviation of the error in the magnitude differences based on all 25 measurements of the nine binary stars in Table 4 is 0.62 mag for the BBM, and is slightly less than the values 0.76 mag and 0.73 mag obtained by least-square fitting the power spectrum (PS) and the bispectrum (BS) respectively. The results appear consistent with the known difficulties in performing photometry of close binary stars. At the same time, some improvement is to be expected with a fine tuning of the detector parameters used during observations - shutter speed, detector gain and frame rate - and by performing measurements under less severe conditions, i.e. with a better and more stable seeing.

To give an example of the outputs of the reconstruction process for STF1909, Figure 4 shows the average power spectrum after calibration with the reference star. In this case, the typical fringes of a double star, with separation very close to the maximum resolving power of the telescope, are clearly visible. The reconstructed image, not corrected for the actual detector orientation, is shown in Figure 5 after convolution with the telescope theoretical PSF.

On a desktop PC with an Intel(R) i3-4130 @ 3.40 GHz processor the required computation time for a selected region of 32 x 32 pixels is less than 5 minutes for 200 iterations, but increases significantly for images of a larger size. In all cases considered,

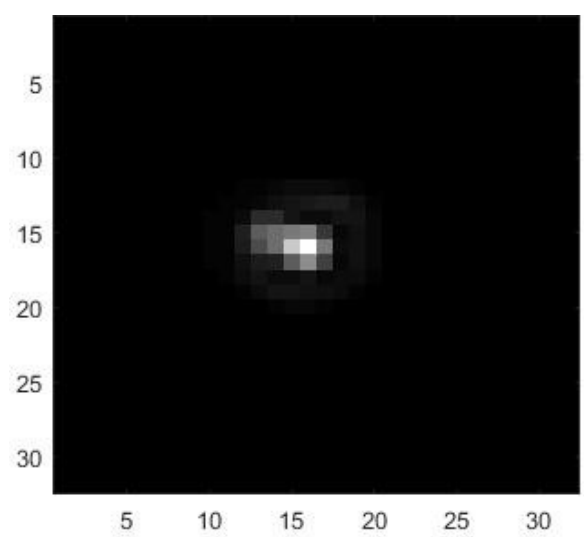

Figure 5: Reconstructed image of STF1909.

Table 4: Estimated binary star parameters vs. known values from the WDS catalog using image reconstruction (BBM) and model fitting both the power spectrum (PS) and bispectrum (BS). The number of observations per night N_{obs} is given in the last column.

Disc	Date	WDS			BBM			PS			BS			Nobs
		ρ(")	θ(°)	Δm	ρ(")	θ(°)	Δm	ρ(")	θ(°)	Δm	ρ(")	θ(°)	Δm	
STT 413AB	2016.479	0.92	359.5	1.53	0.9	359.2	1.63	0.94	1.44	1.36	0.92	1.26	1.13	6
STF1998AB	2016.479	1.09	6.3	0.29	1.09	4.9	0.2	1.11	6.6	0.31	1.09	6.2	0.01	4
STF3050AB	2016.83	2.41	340.6	0.26	2.44	340.8	0.85	2.44	340.8	0.99	2.44	340.9	0.84	2
STF 228	2016.83	0.68	302.1	0.65	0.66	305.8	1.53	0.63	303.6	1.11	0.63	303.4	1.1	2
STF 228	2018.078	0.64	304.6	0.65	0.62	304.2	1.62	0.7	305.1	1.22	0.71	303.5	0.74	2
STF 333AB	2018.078	1.33	209.9	2.65	1.23	209.7	2.24	0.88	205.8	0	0.89	204.48	0	2
STT 215	2018.078	1.57	177.89	0.21	1.5	175.1	1.5	1.54	173.7	1.28	1.48	174.8	1.21	2
STF1687AB	2018.078	1.18	200.16	1.93	1.16	197.7	2.36	1.08	194.1	0.72	1.08	199.8	0.58	2
STF1909	2018.078	0.52	80.84	0.9	0.48	80	0.8	0.41	77.7	0.29	0.44	77.5	0.29	2

less than 50 iterations were required. The plot in Figure 6 shows how the value of the cost function d_k decreases after several iterations in the building block method for STF1909. As a general rule the reconstruction can be stopped once the rate of decrease of d_k reduces significantly.

10. Conclusions

The main concepts involved in the recovery of an image from speckle interferometric data have been reviewed, with some details on how to correct for biases in the power spectrum and bispectrum and on how to calculate the frequency dependent variance of each estimated quantity. The building block method using the bispectrum has been successfully replicated, initially with simulated data and later with the estimate of the separation, position angle and magnitude difference of a number of close binary stars. The obtained accuracy for the magnitude differences is found to be about 0.6 mag with the equipment and the small telescope used in this report, even if some improvement is to be expected under more favorable observing conditions.

Finally, I hope this study and the listed bibliography will also provide a useful starting point to other amateur astronomers interested in the reconstruction of an image from speckles data using the bispectrum.

11. Acknowledgements

The author wishes to thank Carlo Perotti for his support during observations and Karl-Ludwig Bath for useful discussions in the early stages of this work. This research has made use of Cartes du Ciel, the Washington Double Star Catalog, and the double star database Stelle Doppie.

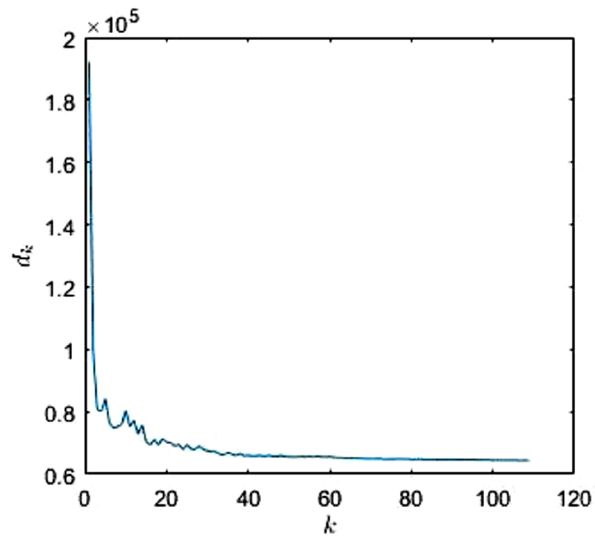

Figure 6. Residual value of the cost function d_k at iteration k in the building block method.

12. References

Bagnuolo, W. G. Jr., Mason, B.D., Barry, D.J., Hartkopf, W.I., and McAlister, H.A., 1992, *Astron. J.*, **103**, 4, 1399-1407.

Caloi, R. M., 2008, *Journal of Double Star Observations*, **4**-3, 111-118.

Genet, R. M., 2015, *Journal of Double Star Observations*, **11**-1S, 266-276.

Goodman, J. W., and J. F. Belsher, 1976, Technical Reports RADC-TR-76-50.

Gordon, J. A., and Buscher, D. F., 2012, *Astron. Astrophys.*, **541**, A46.

Glindemann, A., Lane, R.G., and Dainty, J.C., 1992, *J. Opt. Soc. Am. A*, **9**, 543-548.

Hofmann, K.-H. and Weigelt, G., 1993, *Astron. Astrophys.*, **278**, 328.

Hofmann, K.-H., Weigelt, G. and Schertl, D., 2014, *Astron. Astrophys.*, **565**, A48.

Klein, M.V., and Furtak, T.E., 1986, *Optics*, Wiley.

Labeyrie, A., 1970, *Astron. Astrophys.*, **6**, 85.

Lane, R. G., Glindemann, A., and Dainty, J.C., 1992, *Waves in Random Media*, b (1992), 209-224.

Lohmann, A.W., Weigelt, G., and Wirnitzer, B., 1983, *Appl. Opt.*, **22**, 4028.

McGlamery, B. L., 1976, *Proc. SPIE 0074 Image Processing.*

Pauls, T.A., Young, J.S. Cotton, W.D. and Monnier, J.D., 2005, PASP, **117**, 1255.

Sedmak, G., 2014, *Astron. Astrophys.*, **4**, 155.

Sordiglioni, G., 2012, *Il Bollettino delle Stelle Doppie*, 2.

Thiébaut, É. and Young, J., 2017, *J. Opt. Soc. Am. A*, **34**, 6.

Weigelt, G., 1977, *Opt. Commun.*, **21**, 55.

Wirnitzer, B., 1985, *J. Opt. Soc. Am. A*, **2**,14.